Pore-scale simulation of fluid flow and solute dispersion in three-dimensional porous media

Pore-scale simulation of fluid flow and solute dispersion in three-dimensional porous media

Matteo Icardi

Division of Computer, Electrical and Mathematical Science and Engineering,
King Abdullah University of Science and Technology,
23955-6900, Thuwal, Saudi Arabia and
Institute for Computational Engineering and Sciences,
University of Texas at Austin, 78712-0027, Austin, USA

Gianluca Boccardo and Daniele L. Marchisio*

Department of Applied Science and Technology,
Politecnico di Torino, 10129 Torino, Italy

Tiziana Tosco and Rajandrea Sethi

Department of Environment, Land and Infrastructures,
Politecnico di Torino, 10129 Torino, Italy

(Dated: March 18, 2014)

Abstract

In the present work fluid flow and solute transport through porous media are described by solving the governing equations at the pore-scale with finite-volume discretization. Instead of solving the simplified Stokes equation (very often employed in this context) the full Navier-Stokes equation is used here. The realistic three-dimensional porous medium is created in this work by packing together, with standard ballistic physics, irregular and polydisperse objects. Emphasis is placed on numerical issues related to mesh generation and spatial discretization, which play an important role in determining the final accuracy of the finite-volume scheme, and are often overlooked. The simulations performed are then analyzed in terms of velocity distributions and dispersion rates in a wider range of operating conditions, when compared with other works carried out by solving the Stokes equation. Results show that dispersion within the analyzed porous medium is adequately described by classical power laws obtained by analytic homogenization [1]. Eventually the validity of Fickian diffusion to treat dispersion in porous media is also assessed.

PACS numbers: 47.56.+r, 47.11.Df, 47.10.ad, 05.60.Cd

*Electronic address: daniele.marchisio@polito.it

I. INTRODUCTION

Flow and dispersion processes in porous media are found in many important industrial, biological, and environmental applications and have been studied intensively since many decades. At the microscopic scale (or pore-scale) these phenomena are governed by the fundamental continuity equation, that for an incompressible fluid reads as follows [2]:

$$\nabla \cdot \mathbf{v} = 0, \tag{1}$$

the Navier-Stokes equation:

$$\frac{\partial \mathbf{v}}{\partial t} + \mathbf{v} \cdot \nabla \mathbf{v} = -\frac{\nabla p}{\rho} + \mathbf{g} + \nu \nabla \cdot \left(\nabla \mathbf{v} + \nabla \mathbf{v}^{\mathrm{T}} \right), \tag{2}$$

and the advection-diffusion equation:

$$\frac{\partial c}{\partial t} + \mathbf{v} \cdot \nabla c = \nabla \cdot \left(D_{\mathrm{m}} \nabla c \right), \tag{3}$$

where $\mathbf{v}$ is the pore-scale velocity, p is the fluid pressure, ρ is the density, $\nu = \mu/\rho$ is the kinematic viscosity, μ is the dynamic viscosity, c is the solute concentration and D_{m} is the molecular diffusion coefficient.

The description of this problem is traditionally approached from a macroscopic point of view, by using continuum equations with parameters resulting from averaging procedures carried out on the microscopic structures of the medium (e.g. permeability, porosity) or of the flow (e.g. tortuosity, dispersivity) as explained by Whitaker [3], Berkowitz et al. [4] and Nordbotten et al. [5], resulting in the following continuity equation:

$$\nabla \cdot \mathbf{V} = 0, \tag{4}$$

in the momentum equation:

$$\frac{\partial \mathbf{V}}{\partial t} + \mathbf{V} \cdot \nabla \mathbf{V} = -\frac{\nabla p}{\rho} + \mathbf{g} - \gamma \mathbf{V}, \tag{5}$$

and in the advection-dispersion equation:

$$\frac{\partial (C\epsilon)}{\partial t} + \mathbf{V} \cdot \nabla C = \nabla \cdot \left(\epsilon \mathbf{D} \nabla C \right), \tag{6}$$

where $\mathbf{V}$ is the Darcy velocity (or superficial velocity) and C is the macroscale solute concentration (mass, volume or number concentration of solute in the liquid or void phase).

At low superficial velocities the friction coefficient is assumed to be constant: $\gamma = \mu\epsilon/\rho k$, where ϵ is the porous medium porosity and k is its permeability. In this case, if the time derivative and the inertial terms of Eq. (5), are neglected and the momentum balance equation is applied to a simple one-dimensional problem, the original phenomenological (linear) law developed by Darcy is retrieved. At higher superficial velocities, the Darcy-Forchheimer law is generally used [6–8], and the friction coefficient is assumed to be function of the fluid superficial velocity: $\gamma = \mu\epsilon/\rho\alpha + \beta|\mathbf{V}|$, where now α and β are the two Darcy-Forchheimer parameters. The application of the Darcy-Forchheimer law to a simple one-dimensional problem, again neglecting the time derivative and the inertial terms, results in a quadratic law, often written in the following form:

$$\frac{\Delta P}{L} = 150\frac{(1-\epsilon)^2}{\epsilon^3}\frac{\mu V}{d_{\mathrm{g}}^2} + 1.75\frac{\rho V^2}{d_{\mathrm{g}}}\frac{1-\epsilon}{\epsilon^3}, \tag{7}$$

where ΔP are the pressure drops over the length L of the porous medium considered and V is the superficial velocity along this direction. In Eq. (7) the Darcy-Forchheimer parameters, α and β, are directly expressed in terms of the mean grain size characterizing the porous medium, d_{g}, and its porosity ϵ; the latter equation is known as the Ergun law.

The dispersion tensor $\mathbf{D}$ appearing in Eq. (6) is generally written as the summation of the macroscopic effective molecular diffusion D_0, and of the longitudinal, D_{L}, and transversal, D_{T}, dispersion coefficients [9]. The first (D_0) is the upscaled effect of the molecular diffusion (i.e. it acts even when the fluid is at rest), while the last two are due to mechanical dispersion, caused in turn by velocity inhomogeneities at the pore scale. It is important to notice that, even if the molecular diffusion D_{m} is a scalar, the macroscopic effective molecular diffusion D_0 can become a tensor when the porous medium is not perfectly isotropic. The effect of the system's heterogeneity on particle transport and the importance of diffusive processes occurring at the scale of the pores were noted in several works [10, 11]. In general all these coefficients depend on the porosity of the porous medium, ϵ, on the tortuosity (i.e. a coefficient, τ, or a tensor, $\boldsymbol{\tau}$, that takes into account the geometrical complexity of the medium) and on the Peclét number of the flow (which will be defined later on). The overall effect of diffusion and mechanical dispersion in the porous medium is also called "hydrodynamic dispersion".

Also for the hydrodynamic dispersion, as for the friction coefficient, laws are obtained from experimental investigations and analytical methods and expressed in terms of the rel-

evant dimensionless numbers, as well as the relevant parameters characterizing the porous medium. However, the confidence with which these laws can be employed is not completely clear, especially due to the non-linear dependence between the final macroscale parameters and the initial characteristics of the medium and flow properties. Moreover, the experimental determination of these parameters is often very complicated and affected by large uncertainties.

These issues motivate our research efforts in the explicit simulation of microscale (i.e. pore-scale) flow and hydrodynamic dispersion with the purpose of extracting macroscale laws. In fact, pore-scale simulations can be used to confirm the theoretical and experimental correlation laws and to explicitly compute the constant parameters, usually unknown, for a specific pore geometry. Thanks to the increasing computing resources this analysis is becoming an important area of investigation (see for example [12–22]), with applications into contaminant transport in aquifer, reservoir simulation, CO_2 storage, colloidal transport, chromatographic separation and catalytic reaction engineering [23], recently reviewed by Blunt et al. [24].

The objective of this work is twofold: (i) to analyze the flow and dispersion in a realistic three-dimensional geometry by solving the full Navier-Stokes equation (instead of the often adopted simplified Stokes equation) and (ii) to develop and validate reliable computational tools for the efficient pore-scale simulation in complex geometries, accompanied by the choice of adequate numerical methods and grid convergence tests, as currently done in computational fluid dynamics (CFD). Particular attention is paid here to the well-known mesh generation and spatial discretization issues encountered when Eqs. (1)-(3) are solved with the finite-volume method (FVM). This work is moreover preparatory to the extension of the investigation of particle deposition in porous media from two-dimensional [25] to three-dimensional geometries. Another novelty of this work, beyond the computational tools and strategies adopted, is the usage of an "Eulerian" method to analyze solute dispersion at the pore-scale. We will show that this approach, in contrast to the commonly used tracer particle "Lagrangian" approach, has many computational and practical advantages.

The manuscript is organized as follows. First the macroscopic problem and its classical formulation is briefly recalled and then computational tools developed to extract grain information from real images, reconstruct realistic geometries and discretize the pore space are described. Subsequently the numerical details about the pore-scale simulations are reported

together with the results; simulation predictions are eventually processed to extract velocity distributions and dispersion coefficients, as well as to assess the validity of the Fick law to describe dispersion phenomena. Conclusions and possible next steps are discussed in the last section.

II. RELATIONSHIP BETWEEN MICROSCALE AND MACROSCALE MODELS

The geometry considered in this work is a simple cube filled with grains or particles and immersed in a Newtonian fluid. The fluid flow has one principal direction, indicated with x, with fluid entering and exiting the domain from the faces orthogonal to the x direction and null net fluid flow on the four faces orthogonal to the y and z axes. Starting from the pore-scale velocity, $\mathbf{v}(\mathbf{x})$, and the pore-scale concentration, $c(\mathbf{x})$, fields, by performing a surface average over the y and z directions, the macroscopic (average) Darcy velocity in the main flow direction:

$$V_x(x) = \frac{\int_0^{\mathcal{L}_y} \int_0^{\mathcal{L}_z} v_x(\mathbf{x}) \chi(\mathbf{x}) \, \mathrm{d}y \, \mathrm{d}z}{\mathcal{L}_y \mathcal{L}_z}, \tag{8}$$

and the macroscopic (average) solute concentration:

$$C(x) = \frac{\int_0^{\mathcal{L}_y} \int_0^{\mathcal{L}_z} c(\mathbf{x}) \chi(\mathbf{x}) \, \mathrm{d}y \, \mathrm{d}z}{\int_0^{\mathcal{L}_y} \int_0^{\mathcal{L}_z} \chi(\mathbf{x}) \, \mathrm{d}y \, \mathrm{d}z} = \frac{\int_0^{\mathcal{L}_y} \int_0^{\mathcal{L}_z} c(\mathbf{x}) \chi(\mathbf{x}) \, \mathrm{d}y \, \mathrm{d}z}{\epsilon(x) \mathcal{L}_y \mathcal{L}_z}, \tag{9}$$

are readily defined, where χ is the indicator function of void space, $\epsilon(x)$ is the porosity of the sections, $\mathcal{L}_x, \mathcal{L}_y, \mathcal{L}_z$ are the extensions of the domain in the x, y and z directions respectively, and v_x is the x-component of $\mathbf{v}(\mathbf{x})$. The macroscopic continuity equation (Eq. (4)) becomes the condition of constant macroscopic superficial velocity (or constant mass flux) along the x direction [1, 26, 27]. Based on these definitions one can calculate the deviations of velocity, $v_x' = v_x - V_x/\epsilon$, and concentration, $c' = c - C$, from their average values, and obtain the following macroscopic equation:

$$\frac{\partial (C\epsilon)}{\partial t} + V_x \frac{\partial C}{\partial x} = \frac{\partial}{\partial x} \left(\epsilon D \frac{\partial C}{\partial x} \right), \tag{10}$$

where the other advection terms are null due to the incompressibility condition and the boundary conditions of zero net flux along the y and z directions employed in this work. These boundary conditions also simplify the second-order dispersion tensor $\mathbf{D}$ of Eq. (6), that results in a scalar equal to the summation of the already introduced effective molecular

and longitudinal dispersion coefficients:

$$\left(\epsilon D_0 \frac{\partial C}{\partial x} - \epsilon \langle v_x' c' \rangle\right) = \epsilon D \frac{\partial C}{\partial x}, \qquad \text{with} \quad D = D_0 + D_{\mathrm{L}}, \tag{11}$$

where for the unclosed term $\langle v_x' c' \rangle$ the standard Fick's law was implicitly used:

$$\langle v_x' c' \rangle = \frac{1}{\epsilon \mathcal{L}_y \mathcal{L}_z} \int_0^{\mathcal{L}_y} \int_0^{\mathcal{L}_z} v_x' c' \, \mathrm{d}y \, \mathrm{d}z \approx -D_{\mathrm{L}} \frac{\partial C}{\partial x}. \tag{12}$$

For a detailed derivation of the effective molecular diffusion D_0 and its relation to the microscale molecular diffusion D_{m}, we refer to classical important works [1, 3, 28–30]. When the porosity ϵ is not constant, one can rewrite Eq. (10) as follows:

$$\frac{\partial C}{\partial t} + \left(\frac{V_x}{\epsilon} - \frac{\partial \epsilon D}{\partial x}\right) \frac{\partial C}{\partial x} = \frac{\partial}{\partial x}\left(D \frac{\partial C}{\partial x}\right), \tag{13}$$

where $V_{\mathrm{eff}} = \left(\frac{V_x}{\epsilon} - \frac{\partial \epsilon D}{\partial x}\right)$ takes the role of the effective velocity. The Fickian hypothesis of Eq. (12) can be invalid for more complex porous structures characterized by low porosity, fractures, multi-scale porosity [20, 31]. In these cases, many different models have been proposed such as the fractional advection-diffusion-reaction (ADR) [32, 33] or the continuous-time random walk (CTRW) [34]. Both are based on the generalization of Brownian motion, considering Levy flight processes, while Tartakovsky et al. [35] proposed to introduce a stochastic perturbation in the Darcy equation. For multi-scale porosity media, an extension of Eq. (6) called multiple-rate mass transfer (MRMT) model [36], or the similar mobile-immobile (or dual porosity) model [37] can be used. These models assume the existence of an additional phase and an associated pore space with a different velocity and volume fraction. We refer to the specialized literature cited for more details about these complex models.

Different relationships can be used to estimate D as a function of the Peclét number: $\mathrm{Pe} = V_x d_{\mathrm{g}} / \epsilon D_{\mathrm{m}}$. For Pe tending to zero the following relationship holds [1]:

$$\frac{D}{D_{\mathrm{m}}} = \frac{1}{\tau^2}, \tag{14}$$

where τ is the tortuosity of the porous medium. Many definitions and formula have been proposed and recent works [38–40] have demonstrated their effectiveness and the difference between formulations. The most common definition involves the computations of streaklines (i.e. Lagrangian trajectories) of the flow and the calculation of the ratio between their length

and the porous medium size. Koponen et al. [38] and Duda et al. [40] proposed a simpler way to compute τ as a volume integral

$$\tau = \frac{\int |\mathbf{v}| \, \mathrm{d}\mathbf{x}}{\int v_x \, \mathrm{d}\mathbf{x}}. \tag{15}$$

A widely used correlation for the hydrodynamic dispersion at higher Pe numbers is: $D = \alpha V_x$, where α is of the order of the mean grain size. van Milligen and Bons [41] derived a single equation valid for different ranges of Pectlét numbers:

$$\frac{D}{D_\mathrm{m}} = \frac{\gamma + \beta \frac{\mathrm{Pe}^2}{\mathrm{Pe_c}}}{1 + \frac{\mathrm{Pe}}{\mathrm{Pe_c}}}, \tag{16}$$

where $\mathrm{Pe_c}$ is the critical Pe number, γ is the coefficient that scales the macroscale dispersion, D, to the molecular diffusivity, D_m, for $\mathrm{Pe} \ll 1$ whereas β is the linear coefficient between D, D_m and Pe for $\mathrm{Pe} \gg 1$. The three asymptotic regimes can be identified by defining $\delta = \sqrt{\frac{\gamma}{\beta}}$:

$$D \approx \begin{cases} \gamma D_\mathrm{m} & \text{when} \quad \mathrm{Pe} \ll \delta\sqrt{\mathrm{Pe_c}} \\ \beta \mathrm{Pe}^2/\mathrm{Pe_c} & \text{when} \quad \delta\sqrt{\mathrm{Pe_c}} \ll \mathrm{Pe} \ll \mathrm{Pe_c} \\ \beta \mathrm{Pe} & \text{when} \quad \mathrm{Pe} \gg \mathrm{Pe_c}. \end{cases} \tag{17}$$

This simple relationship is not universally valid, in fact, it typically does not hold for more complex porous media (where, for example, a non-linear relation can appear for high Peclét number) and in the pre-asymptotic regime. Another common expression is the correlation proposed by Bear [1]:

$$\frac{D}{D_\mathrm{m}} = \gamma + \frac{\alpha V}{D_\mathrm{m}} \frac{\mathrm{Pe}}{\mathrm{Pe} + 2 + 4\delta^2}, \tag{18}$$

where γ and δ have the same physical meaning of the coefficients appearing in Eq. (17).

III. THREE-DIMENSIONAL GRAIN PACKING AND MESH GENERATION

In this section the strategy employed to create the three-dimensional porous medium used in this work and the mesh generation procedure for performing the finite-volume discretization are briefly described.

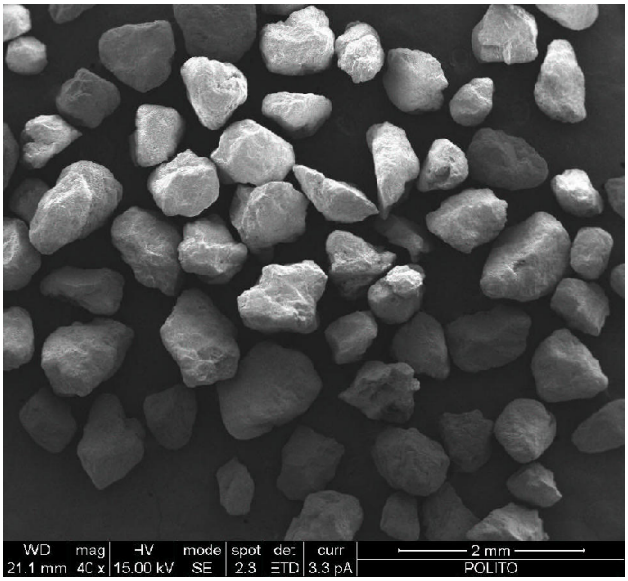

FIG. 1: SEM image of the real sand sample used to extract grain size distribution and approximate the grain shapes.

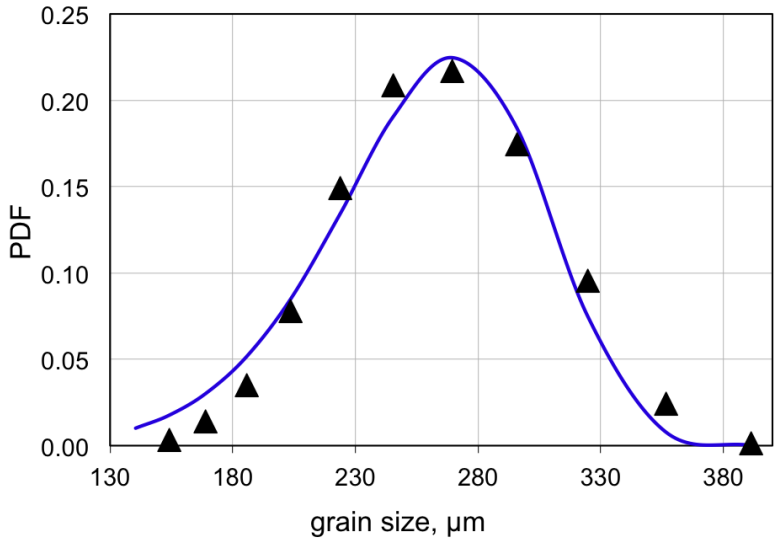

FIG. 2: Grain size distribution of the sand packing under study (black dashed line with triangles) and approximation with Weibull distribution (continuous blue line with circles).

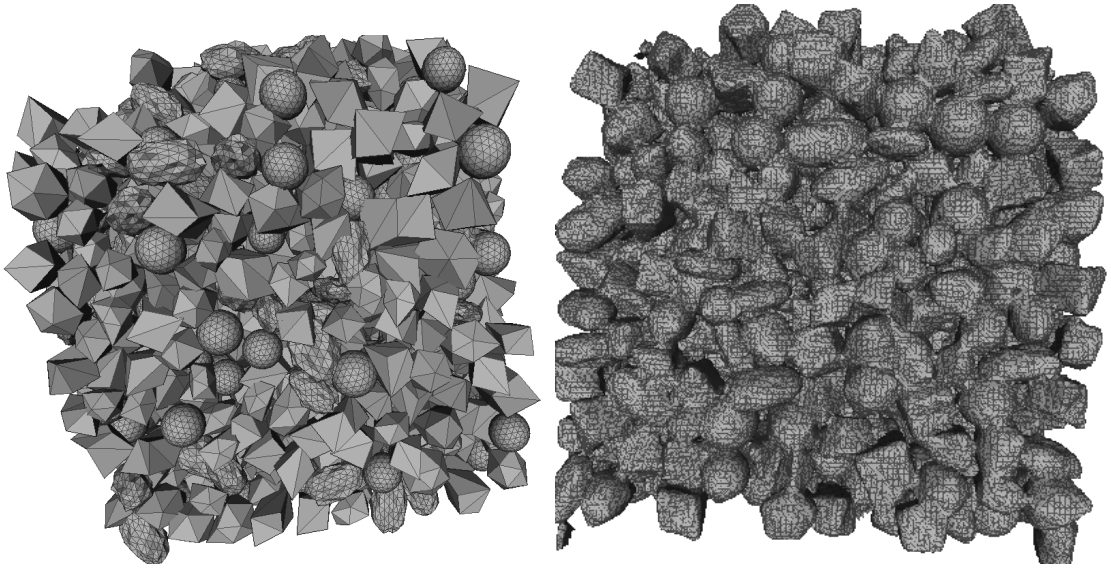

FIG. 3: Mesh re-sampling, randomization and regularization. Original surface mesh (left) and re-sampled mesh (right).

A. Grain packing generation

The first necessary step requires to build a representative microscopic model of a porous medium sample in order to simulate fluid flow in these systems. There are many ways to obtain such a model: the first choice is between real sand sample images, for example experimentally acquired by micro-computer tomography techniques, and realistic reconstructions by means of suitable algorithms [24]. Although the former provides representations of the pore microstructure which are real, the extraction procedures (segmentation, surface reconstruction, etc.) are usually quite complicated, expensive and with a high degree of arbitrariness. Therefore, it was chosen to reconstruct a realistic porous medium with ad-hoc algorithms. It has to be noted that when following this approach one has to make sure that the characteristics and features of the generated porous medium (e.g. porosity, grain size distribution and pore-throat structure) are representative of a real system. Notwithstanding these difficulties, there are several advantages with this approach; it is possible, for example, to test simple geometries (where real grains are modeled as spheres) that make it easier to study multiple test cases (e.g. models with different grain diameter or porosity) in a semi-automatic fashion [25].

A number of methods have been proposed to synthetically generate realistic packed

geometries. Some of them are based on the idea of representing the medium with a pore-network model, whereas some others "reconstruct" the entire structure of the porous medium, down to the single grains, using different algorithms (i.e. random sequential adsorption, gravitational deposition, collective arrangement, binary random fields) [42–47]. In this work, two different methods of packing generation, both based on the open-source library Bullet Physics [48], were tested: SettleDyn [49] and Blender [50]. The tested methods simulate the sedimentation of real three-dimensional grains, represented by convex polygonal surface meshes, generating loose sand-like structures from given particle forms and grain size distributions.

The first step is the definition of grain shape and grain size distribution, that in this work were obtained respectively by two-dimensional scanning electron microscopy (SEM) scans (see for example Fig. 1) and static-light scattering measurements carried out on standard sand samples. For the case investigated in this work the final mean grain size d_{50} was equal to 0.277 mm. The grain size distribution was then fitted with a Weibull distribution [7, 25], resulting in a shape parameter equal to seven and was then randomly sampled when creating the packing. Figure 2 compares the experimentally measured grain size distribution of the sample with the reconstructed Weibull distribution.

Different confined packings of thousands of grains were then generated, by randomly sampling the Weibull distribution, on a single core machine, with large quantity of memory in a few hours. These tests highlighted, for the operating conditions investigated in this work, a higher flexibility when using Blender, especially in terms of robustness and convergence. One of these packings (created with Blender) with more than 3000 grains, was extensively used in this work for most of the pore-scale simulations. The final optimized porous medium is a cube domain of 2.1 mm length and is characterized by an average porosity of 0.35. By splitting the geometry in ten sub-volumes along the x-axis, it was noted that the porosity (in these sub-volumes) fluctuates around this value by approximately 1%, while the porosity calculated on the surfaces varies between 0.31 and 0.39.

B. Mesh generation

After the generation of the grain packing, the geometric representation (made of polygonal surface mesh) of the resulting grain packings was cleaned through mesh re-sampling, in order

to remove intersections and artifacts. This was done with the marching cubes algorithm [51, 52]. An example is reported in Fig. 3, that shows a surface mesh, obtained with the algorithms previously described and grains characterized by very sharp edges, and the final re-sampled mesh. After re-sampling the pore domain is ready to be discretized through body-fitted meshes, as commonly done when the FVM is used.

As mentioned before, great care was put forward during the pre-processing phase of this work in order to ensure the highest possible accuracy with respect to numerical and computational issues. A careful analysis of the mesh generation process now follows, along with the description of the steps taken to ascertain the validity of the final mesh thus obtained.

The mesh utility `snappyHexMesh`, native to the open-source package `OpenFOAM` [53], was used. Grid building was performed in two steps. First, a structured, cartesian mesh was created in the fluid portion of the domain, in order to minimize average non-orthogonality and skewness in the final mesh. The handling of the actual surface of the solid part in this initial step is done in a way similar to how immersed boundary meshes are constructed, resulting in a step-wise approximation of the grains. However, a precise reconstruction of the actual grain geometry was deemed essential in this work, thus requiring a second step in which the mesh was modified by means of relocating boundary vertices, resulting in a body-fitted mesh. A visual aid for the description of this process is found in Fig. 4.

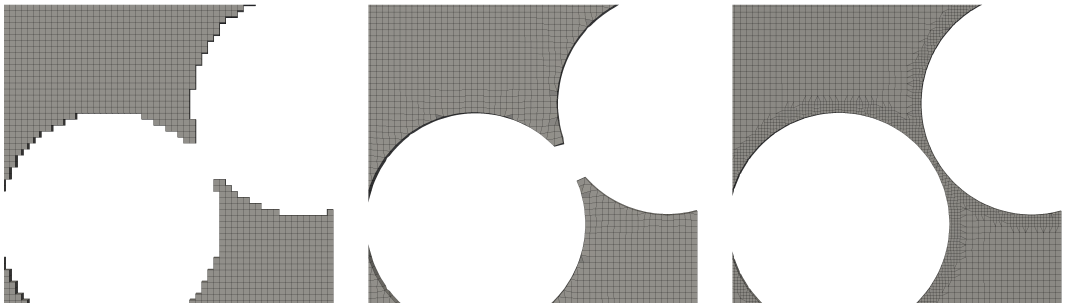

FIG. 4: Details of the mesh refinement process. Step-wise castellation (left), body-fitting via vertices moving (center) and precise geometry reconstruction with subsequent mesh refinements (right).

In addition to these two steps, one of the subsequent grid refinement steps is also visualized. In fact, the most critical operation was the construction of a mesh of high quality to

ensure grid independent results. To this end, a number of refinements were performed, and two parameters monitored throughout in order to quantitatively assess the resulting mesh suitability for use with the CFD code. Given the heavy computational resources required for the CFD calculations (as described in the following sections), these tests were not performed on the full domain used for the production runs, but rather on two smaller sub-volumes. The linear dimensions of each of these volumes are smaller by a factor of four with respect to the complete geometry, resulting in 500 μm $\times$ 500 μm $\times$ 500 μm cubes. This is shown in Fig. 5.

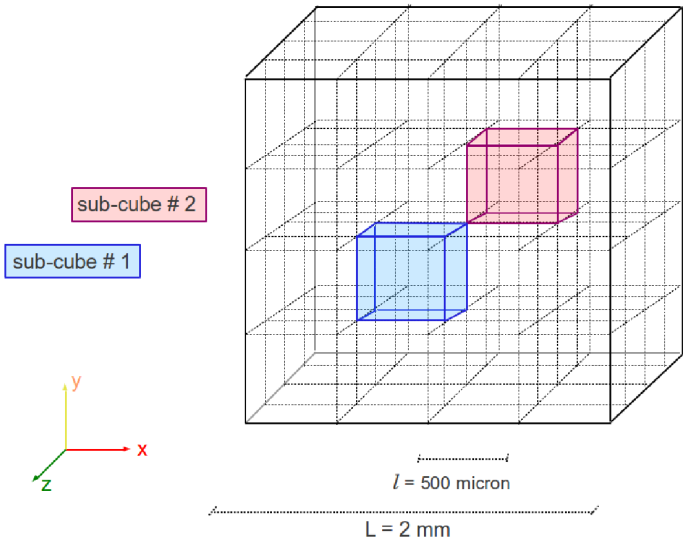

FIG. 5: Complete geometry bounding box and location of the two sub-volumes chosen for the grid independence analysis.

An outline of all the mesh modification steps, along with the calculated relevant parameters associated with each test (for one of the two sub-volums), is reported in Tab. I. As a qualitative description of these cases, the first two represent the starting uniform mesh and a uniform refining thereof, respectively. The following cases differ by representing progressive

Case	Mesh cells (thousands)	ϵ , -	d_g^* , μm
U1	37	0,3025	203,0
U2	308	0,3088	207,8
B1	1.218	0,3102	217,4
B2-IC	2.284	0,3104	214,9
B2.5	3.539	0,3105	216,1
B3	5.053	0,3105	215,6

TABLE I: Number of mesh cells, porosity and effective grain diameter (μm) for each of the grid refinement steps.

refinement of mesh cells size near the border of the grains, with this region being chosen in order to increase the precision in the description of the momentum and particle concentration boundary layers, where the gradients of these properties will be stronger. The first of the two properties of interest being monitored at this stage is the porosity: as it can be seen from Tab. I its value changes (increasing slightly) with the increase in the number of cells. This is due to the addition of more cells near the surface of the grains allowing not only for a better numerical solution, but also for a more precise reconstruction of the actual porous medium geometry. Again, Fig. 4 exemplifies this process. The fourth case (B2-IC) reaches a satisfactory description in such respect. The other parameter needed to assess the grid independence of the results for the flow field is the equivalent diameter d_g^*. Following the same methodology applied in a previous work (and described in details therein [25]), for each level of grid refinement steady-state flow field simulations at different superficial velocities were run, and the pressure drop results compared with the predictions of the Ergun law for that system (see Eq. (7)). Treating the grain diameter as a fitting parameter, the effective diameter d_g^* reported in Tab. I results from the closest fitting of the obtained CFD results with the theoretical predictions. Considering the variation of d_g^* with increasing mesh cells number, again the fourth case provides a good resolution of the momentum boundary layer, as the heavy mesh refinements performed in the subsequent cases correspond to negligible changes in effective grain diameter. Thus, the mesh for the complete geometry used in the final runs, from which all the results presented in this work were obtained, was built in such a way to result in the same features as those identified in the case B2-IC of Tab. I.

IV. NUMERICAL DETAILS OF THE CFD SIMULATIONS

The flow field in the reconstructed geometry was simulated with the open-source code `OpenFOAM`. The three-dimensional incompressible steady Navier-Stokes equations were solved with the `simpleFoam` solver. As mentioned the equations were discretized with the FVM. The numerical schemes used were chosen in order to minimize the numerical errors for the different test cases characterized by a wide range of Reynolds numbers (see Table II). A second-order central scheme with limiters to avoid oscillations was used for spatial discretization and the SIMPLEC scheme was used to overcome the pressure-velocity coupling problem.

The whole cubic domain, extracted by the packing and reported in Figs. 3 and 5, was studied with a fixed hydraulic head drop between inlet and outlet and with symmetric conditions on the lateral boundaries. This means that the resulting main flow is directed along the x-axis and there is no flow escaping from lateral boundaries (in the y and z directions). The simulated domain length was $\mathcal{L}_x = \mathcal{L}_y = \mathcal{L}_z = 2$ mm and it contained about three thousands sand grains. For each value of hydraulic head drop, the mean flow rate and Darcy fluxes V_x were calculated in sections of the porous medium orthogonal to the mean flow field. A summary of the resulting Reynolds, $\mathrm{Re} = d_{50}V_x/\epsilon\nu$, and Peclét numbers, $\mathrm{Pe} = d_{50}V_x/\epsilon D_{\mathrm{m}}$, is reported in Table II; both dimensionless numbers are evaluated by using $d_{50} = 0.270$ mm as en estimation of the grain size d_{g}. As it is seen, the flow fields obtained at different Reynolds numbers were used to transport an Eulerian solute concentration field with different molecular diffusion coefficients resulting in Peclét numbers ranging from 10^{-2} up to 10^{6}.

The simulations of the flow field were carried out in parallel on a Linux workstation with 12 Intel Xeon X6960 cores. The computational bottle-neck for these simulations turned out to be the huge memory usage (100GB), rather than the convergence iterations (usually less than 100). In our configuration this resulted in 12 hours of total CPU time for each flow field computation.

The simulations of solute transport were carried out in `OpenFOAM` but with a unsteady solver, up to the full saturation of the medium. A constant concentration (constant Dirichlet boundary conditions with a fixed concentration equal to unity) was employed as boundary condition at the inlet. A null concentration gradient was instead used as boundary condition

on the grain surfaces (neglecting therefore particle deposition) and on the lateral and outlet boundaries (approximating an infinite medium). These more computationally demanding simulations were carried out in parallel on the Curie supercomputer, owned by GENCI and operated by CEA, using 48 Intel Nehalem-EX X7560 cores. In our configuration this resulted in 240 hours of total CPU time for each scalar transport computation. The domain was decomposed by simple splitting the domain in each direction by powers of two. Scalability tests were performed for the flow solver and for the scalar transport, showing that, even if the three-dimensional mesh is highly irregular and unstructured, it is possible to reach an almost linear speed-up up to 512 cores, excluding the I/O operations. Due to the high Peclét number flows a second-order limited upwind space discretization with second-order Crank-Nicholson time stepping was used to solve the solute concentration transport equation (i.e. Eq. (3)).

V_x, m s^{-1}	Re	Pe		
		$D_\mathrm{m} = 5 \times 10^{-11}$, m^2 s^{-1}	$D_\mathrm{m} = 5 \times 10^{-10}$, m^2 s^{-1}	$D_\mathrm{m} = 5 \times 10^{-9}$, m^2 s^{-1}
1.2×10^{-7}	9.6×10^{-5}	1.9×10^{-2}	1.9×10^{-1}	1.9×10^{0}
1.2×10^{-6}	9.6×10^{-4}	1.9×10^{-1}	1.9×10^{0}	1.9×10^{1}
1.2×10^{-5}	9.6×10^{-3}	1.9×10^{0}	1.9×10^{1}	1.9×10^{2}
1.2×10^{-4}	9.6×10^{-2}	1.9×10^{1}	1.9×10^{2}	1.9×10^{3}
1.2×10^{-3}	9.6×10^{-1}	1.9×10^{2}	1.9×10^{3}	1.9×10^{4}
1.2×10^{-2}	9.2	1.8×10^{3}	1.8×10^{4}	1.8×10^{5}
8.3×10^{-2}	66	1.3×10^{4}	1.3×10^{5}	1.3×10^{6}
3.9×10^{-1}	314	6.1×10^{4}	6.1×10^{5}	6.1×10^{6}

TABLE II: Superficial flow velocities, V_x, Reynolds numbers, Re, molecular diffusion coefficients, D_m, and resulting Peclét numbers, Pe.

V. RESULTS AND DISCUSSION

In what follows the results of our simulations are presented, focusing first on the flow field predictions, and subsequently on the solute transport predictions.

A. Fluid flow

Figure 6 reports a typical example of the flow field inside the porous medium for a Reynolds number of 9.6×10^{-3}. We begin our analysis by plotting the normalized pressure drops, $\Delta p/\rho V_x^2 \mathcal{L}_x$, versus the normalized Darcy velocity, V_x/ν, resulting in the well known behavior reported in Fig. 7. As expected two domains are identified, one at low Darcy flux values corresponding to the region of validity of the Darcy law (and a linear behaviour in this graph), and a second one at higher values of Darcy flux where this law is not valid anymore. From the slope of the curve (in the first linear region) an intrinsic permeability of 4.0×10^{-8} cm^2 can be obtained. By using Eq. (15), the tortuosity, τ, was estimated in our case to be equal to 1.2 for low Re. However, for Reynolds numbers greater than ten it increases and reaches the value of 1.7 for Re = 314. This is due to the different flow conditions in the pore space arising at higher velocities, changing the trajectories of the moving fluid and thus τ.

Further analysis of the simulation data requires some upscaling, for which different methodologies were proposed and we refer to the work of Cushman et al. [54] for an overview. In the present work simulation results were analyzed by both volume-averaging on the whole three-dimensional domain and by surface-averaging on ten equispaced sections orthogonal to the main flow direction x. In addition to that these ten surfaces were also used to evaluate how relevant properties are spatially distributed.

For example, by analyzing how the fluid velocity differs from point to point on these ten surfaces, the data reported in Fig. 8 and Fig. 9 were obtained. These figures show the velocity distributions for the x, y and z fluid velocity components, in three of the ten sections investigated, for two superficial velocities, resulting in Reynolds numbers of Re $= 9.6 \times 10^{-3}$ and of Re = 66, respectively. The histograms were computed with 1000 random samples on each surface and are reported in logarithmic scale. As it is possible to see from Fig. 8, the velocity distribution for the x component has a maximum corresponding to the superficial velocity, V_x, but highlights in the section regions where the fluid moves with different velocities. Comparison of these distributions with the equivalent Gaussian distributions (that share the first three moments) highlights a much higher frequency of velocities close to the mean value and, at the same time, the existence of larger tails of the distributions. Closer observation of the distributions in the y and z directions leads to similar conclusions, with the only difference that now these distributions are centered on

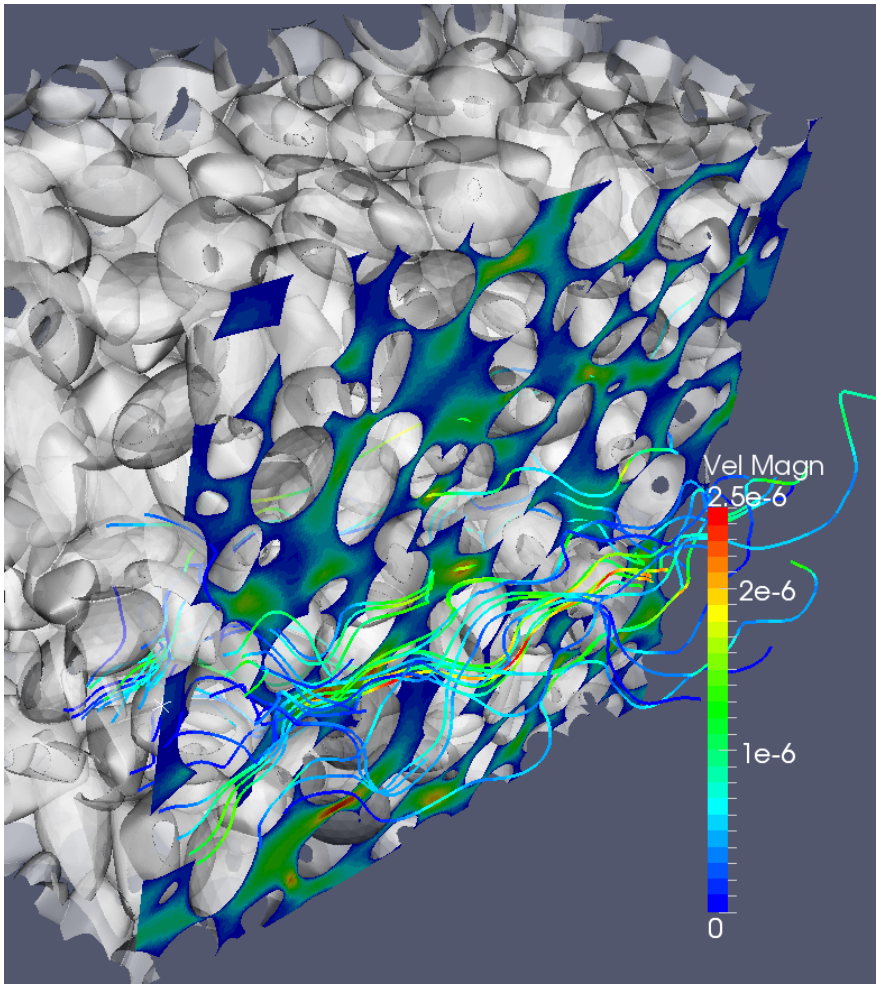

FIG. 6: Visualization of the flow field in the porous medium for Re $= 9.6 \times 10^{-3}$. Velocity magnitude is computed in a central slice and some flow streamlines are shown.

zero (as there is no net flux in these directions) and exhibit a certain symmetry and a shape slightly closer to that of a Gaussian distribution. When the superficial velocity is increased the situation observed is very similar (see Fig. 9) to the previous one, as in this case the distributions are simply characterized by larger variances.

B. Hydrodynamic dispersion

To quantify the effect of these distributions in generating dispersion phenomena in the porous medium, let us analyze the results of the solution dispersion simulations. One typical result is reported in Figure 10, where the normalized solute concentration at three instants

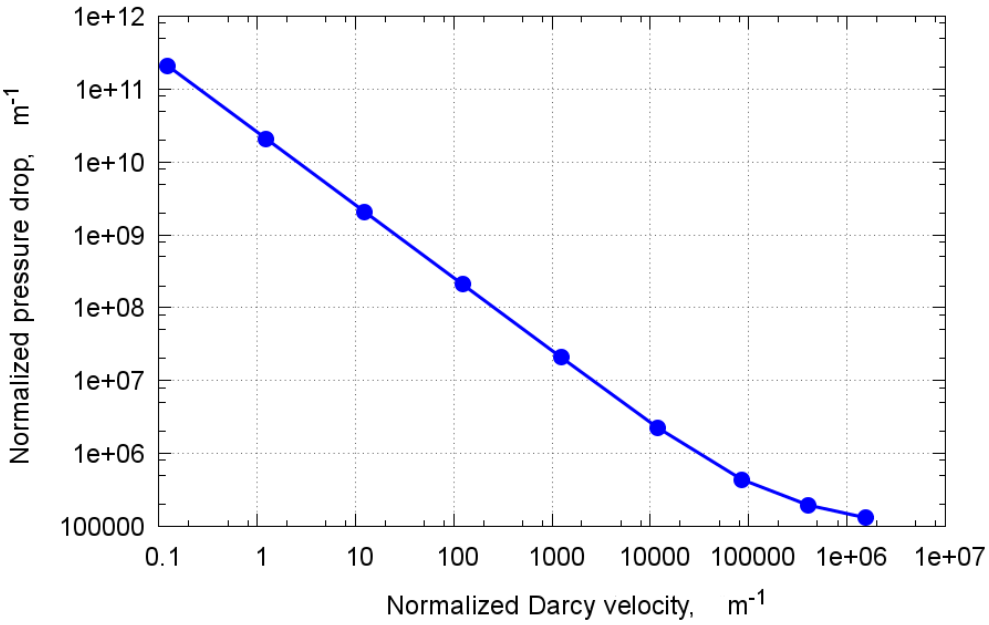

FIG. 7: Normalized pressure drops, $\Delta p/\rho V_x^2 \mathcal{L}_x$, versus normalized superficial velocity, V_x/ν. The slope of the first part of the curve represent the inverse of the permeability of the medium.

of the simulation is reported. As it is seen, as the solute moves downstream hydraulic dispersion takes place and the concentration front becomes more and more smoothed out.

As already said, the three-dimensional results were surface-averaged on sections perpendicular to the main flow direction, and, among other variables, the average solute concentration in these sections was tracked versus time. The resulting time-evolution curves (known as breakthrough curves) were then used to characterize the dispersion dynamics in the medium. Three typical results for different Re and Pe numbers are reported in Fig. 11, for nine equidistant sections, from $x = 0.15\mathcal{L}_x$ to $x = 0.95\mathcal{L}_x$ (to avoid boundary effects).

The breakthrough curves reported in Fig. 11 with continuous lines correspond to three different regimes. In the first one (top) molecular diffusion is prevailing over advective transport, in the second and third ones (middle) the two effects are of the same order of magnitude, while in the fourth one (bottom) molecular diffusion can be neglected with respect to advection. Due to the small changes in porosity of the sections, some of the curves of contiguous sections overlap.

The concentration transport at the macroscale (as sketched in Fig. 11) should obey to the macroscopic advection-diffusion equation reported in its general form in Eq. (6) and for

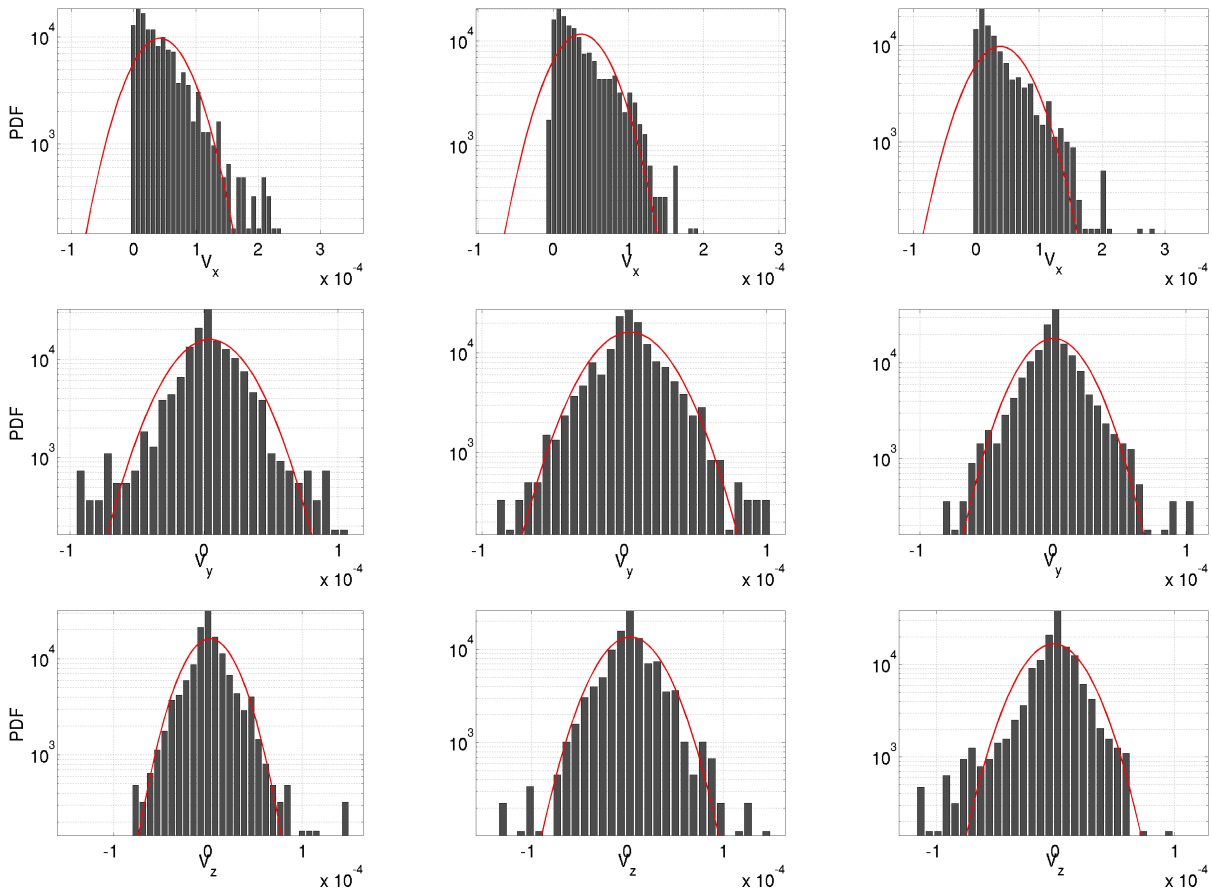

FIG. 8: Velocity distributions for Re $= 9.6 \times 10^{-3}$ and for, from top to bottom, the x-, y-, and z-components and for, from left to right, the first, fourth and tenth section. The histogram corresponds to the actual distribution as calculated from the simulations, whereas the red curve is the Gaussian distribution with identical first three moments.

the problem investigated in this work, Eq. (6) takes the one-dimensional form reported in Eq. (13), whose coefficients are in turn unknown. Neglecting the presence of a possible stagnant phase or a retardation factor, the only actual unknown parameter is the hydrodynamic dispersion. However, also the effective transport velocity (V_{eff}) was included as a unknown parameter, to check the validity of the transport equation. Since we are considering a volume comparable to the representative elementary volume, there are not enough data along the x-direction, but temporal data can be indeed considered (for fixed spatial locations).

The two unknown parameters (i.e. V_{eff} and D) were computed with two methods. The first method is based on the inverse problem formulation. Given the breakthrough curves (concentration over time), the effective parameters are estimated with non-linear least square

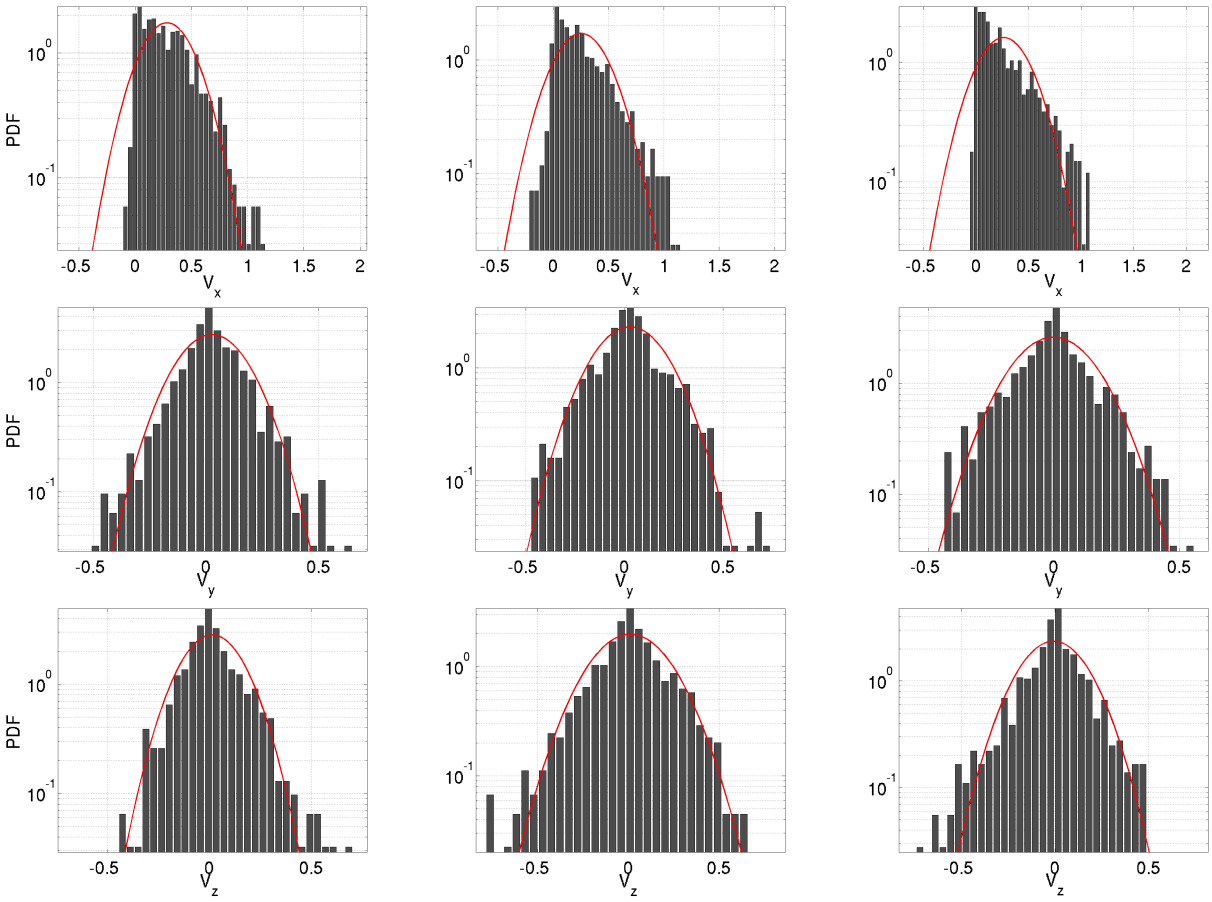

FIG. 9: Velocity distributions for Re = 66 and for, from top to bottom, the x-, y-, and z-components and for, from left to right, the first, fourth and tenth section. The histogram corresponds to the actual distribution as calculated from the simulations, whereas the red curve is the Gaussian distribution with identical first three moments.

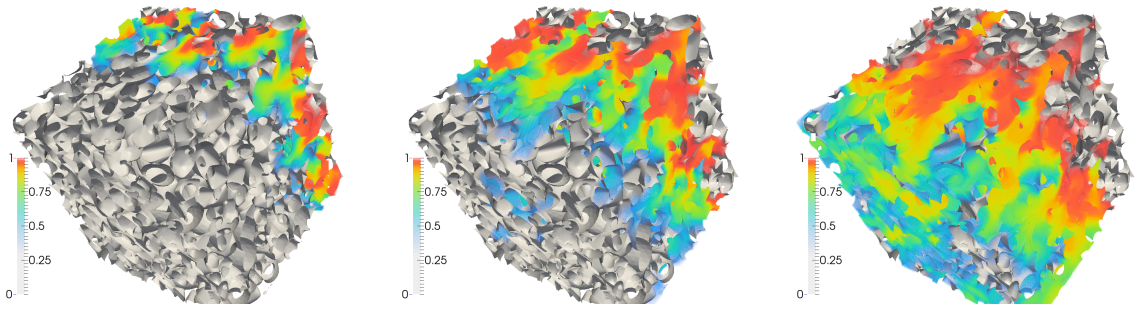

FIG. 10: Contour plots of the solute concentration in the porous medium at three instants of the simulation for Pe = 1.9×10^3.

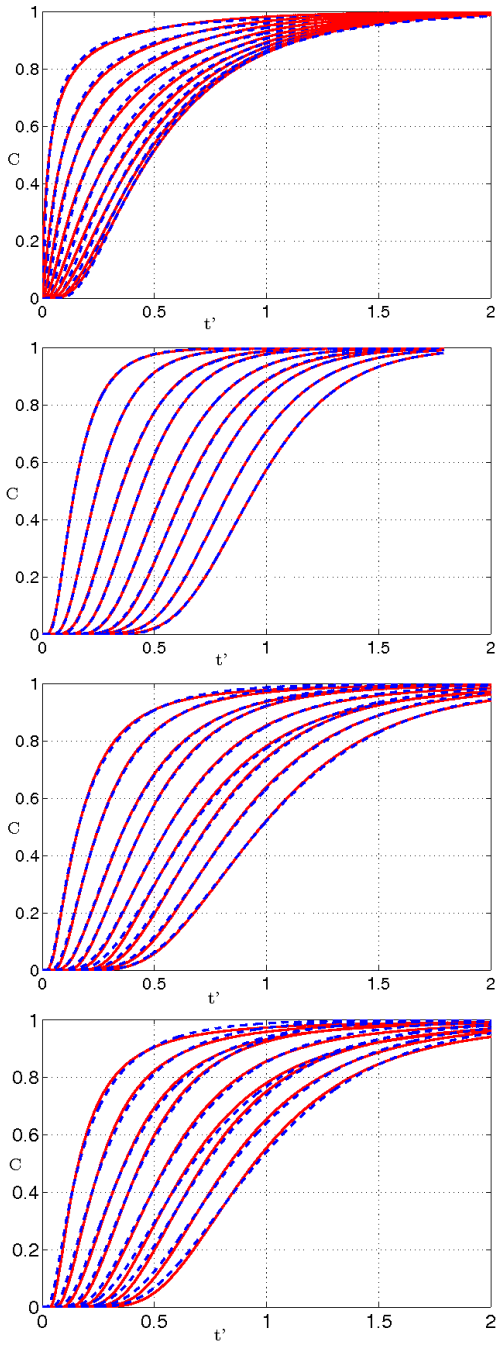

FIG. 11: Comparison between breakthrough curves (normalized solute concentration, continuous red line) over dimensionless time $t' = t\epsilon/V_x$ obtained by surface-averaging over equidistant sections of the porous medium for different Peclét numbers (from top to bottom, $\mathrm{Pe} = 1.9 \times 10^{-1}$, $\mathrm{Pe} = 1.9 \times 10^{1}$, $\mathrm{Pe} = 1.9 \times 10^{3}$, $\mathrm{Pe} = 1.3 \times 10^{5}$) with the analytic solutions of the semi-infinite advection-diffusion equation with the fitted parameters (dashed blue line).

minimization using standard optimization techniques. The second strategy is instead based on the method of moments [55], where the unknown parameters are calculated from the first three normalized centered temporal moments at the outlet of the computational domain:

$$M_0 = \int_0^\infty g(x = \mathcal{L}_x, t)\,\mathrm{d}t; \quad M_1 = \int_0^\infty \frac{g(x = \mathcal{L}_x, t)t}{M_0}\,\mathrm{d}t; \quad M_2 = \int_0^\infty \frac{g(x = \mathcal{L}_x, t)t^2\,\mathrm{d}t}{M_0} - M_1^2, \tag{19}$$

where $g(x,t)$ is the Green function of Eq. (6) (i.e. the solution for a Dirac delta boundary condition centered at $x = 0$ and $t = 0$). The effective velocity is then given by:

$$V_{\text{eff}} = \left(\frac{\epsilon \mathcal{L}_x}{M_1}\right), \tag{20}$$

whereas the dispersion coefficient is given by:

$$D = \frac{M_2}{2\mathcal{L}_x}\left(\frac{V_x}{\epsilon}\right)^3. \tag{21}$$

This method in general performs better for the estimations of porosity (or equivalently the Darcy fluxes) and hydrodynamic dispersion in terms of computational time, accuracy and stability. Since the two methods resulted, however, in very similar (if not almost identical) results, only the parameters estimated with the method of moments will be shown and discussed.

Figure 12 shows the estimation of the effective velocity (V_{eff}) divided by the value of V_x computed from the averaging for the different Peclét numbers. As it can be seen, the effect of diffusive flux (see Eq. (13)) is important for low Peclét numbers when they can be order of magnitudes larger than the advective fluxes. When this effect is no more visible (i.e. for high Peclét numbers), the estimated velocity is always slightly lower than the theoretical one. This is clearly explained by Eq. (13) where the gradient of porosity appears as an additional convective flux (in our case in fact the porosity in the last sections used for the fitting is about 3% lower than the initial one).

Figure 13 shows the estimated dispersion coefficients D divided by the molecular diffusion coefficient D_{m} for the different Peclét numbers investigated. It should be observed that the scaling of D/D_{m} with the Peclét number reproduces many recent computational results and classical power laws (obtained in turn by experimental and theoretical studies [29, 31, 56]). As it is seen a constant behavior is observed in the first region (very low Pe), followed by a superlinear relationship (with an exponent of 1.2) in the central part, and a linear scaling at very high Pe in the last part.

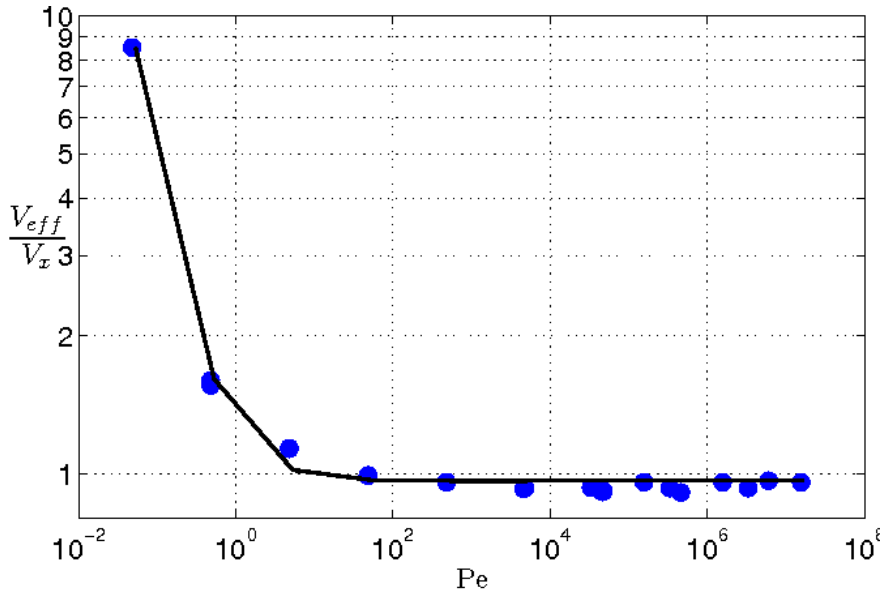

FIG. 12: Effective transport velocity, as estimated by the method of moments.

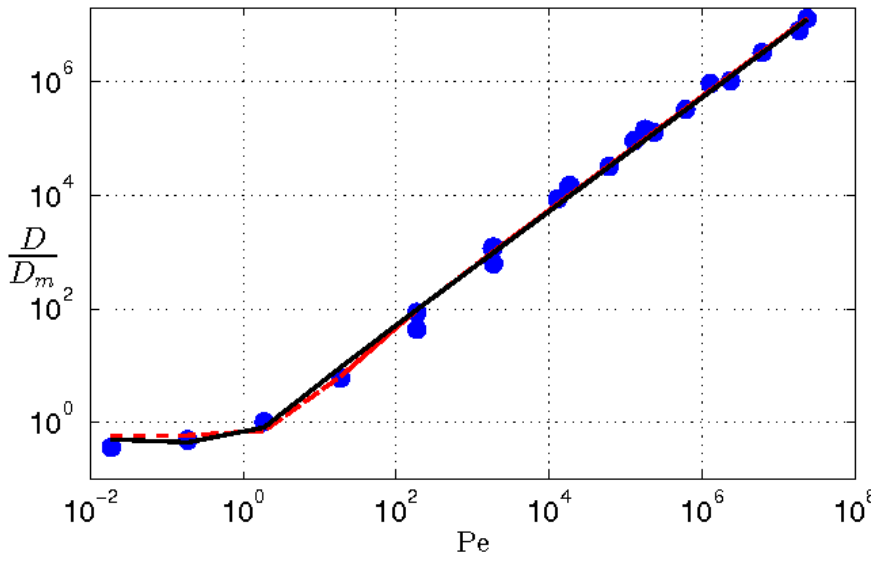

FIG. 13: Dispersion coefficients for different Peclét numbers, as estimated by the method of moments (blue crosses) together with two fitted correlation laws; the continuous black line is Eq. (17) whereas the dashed red line is Eq. (18).

It is interesting to notice that in the constant part (Pe $\rightarrow$ 0) of the plot, the result of Eq. (14), is confirmed. In fact, for this system the tortuosity was quantified to be about 1.2, resulting in a ratio between D and D_{m} of about 0.69 (as observable in Fig. 13). Considering the linear regime (high Peclét numbers) the already introduced expression: $D = \alpha V_x$, was found to be an adequate description for our medium; the constant α was estimated to be between 60 and 90 % of d_{50}, depending on the Peclét number.

Eventually, if the data of D/D_{m} versus Pe are fitted with the laws reported in Eqs. (17) and (18), the following results are obtained. The fitted parameters for Eq. (17) are: $\gamma = 0.51$, $\beta = 0.52$ and $\mathrm{Pe_c} = 0.99$, whereas for Eq. (18) are: $\gamma = 0.59$, $\alpha = 1.52 \times 10^{-4}$, and $\delta = 1.76$. It is interesting to highlight that the coefficient γ estimated with these two correlations are in good agreement with each other and with the estimation of tortuosity given by Eqs. (14) and (15). Both laws are reported (with these values of γ, α, β, δ and $\mathrm{Pe_c}$) in Fig. 13 together with our simulation results.

At last it is interesting to verify the validity of Fickian diffusion, that was used to close Eq. (12). In order to perform this analysis the quantity $\langle v'_x c' \rangle$, reported on the left-hand side of Eq. (12), was calculated and compared with the quantity reported on the right-hand side of Eq. (12) for ten different sections. This latter quantity is the product of the dispersion coefficient and the gradient on the main flow direction (x) of the surface-averaged concentration, $C(x)$, or in other words the dispersive flux as approximated by Fick's law, with the value of D_{L} calculated with the fitting performed with the method of moments. Typical results of this analysis for two superficial velocities are reported together with the dispersive fluxes at four different instants of the simulations in Fig. 14 and, as it is possible to see, the two curves are very close at low superficial velocity ($\mathrm{Re} = 9.6 \times 10^{-3}$). Larger deviations from the theoretical Fickian behavior are noticeable for higher velocities (Re = 66), where vorticity and wakes develop more extensively. However, for both cases the hypothesis of Fickian behavior can be safely assumed.

VI. SUMMARY AND CONCLUSIONS

Pore-scale simulations of single phase flows and scalar transport have been carried out by means of CFD with high-order numerical schemes and advanced meshing techniques. Wide ranges of Reynolds (from 10^{-4} to 10^{2}) and scalar Peclét (from 10^{-2} to 10^{6}) numbers

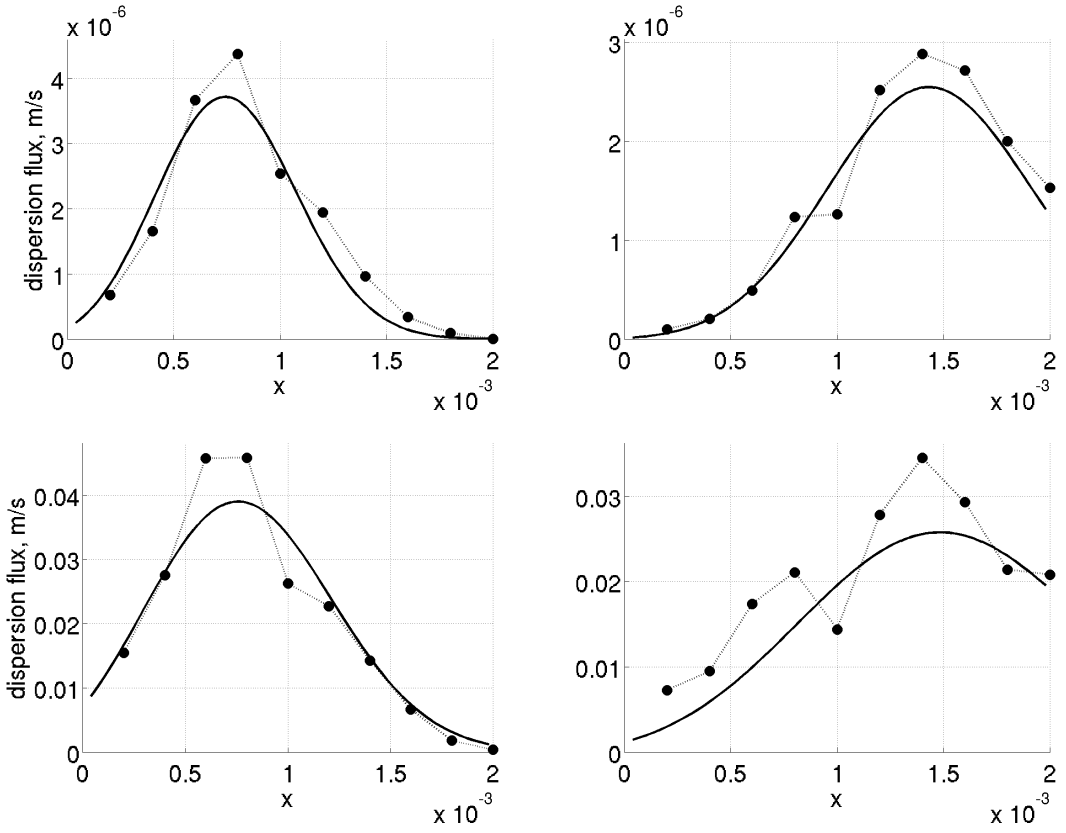

FIG. 14: Comparison of the dispersion flux $\langle v_x' c' \rangle$ as calculated from the three-dimensional simulations (dotted lines with symbols) and as approximated by Fick's law (computed as the spatial derivative of the analytic solution for semi-infinite media with the fitted parameters, continuous line) for two different Reynolds numbers (top: Re $= 9.6 \times 10^{-3}$; bottom:Re $= 66$) and at two instants (from left to right).

have been investigated, including non-linear regimes. Results from steady-state (for flow field) and transient (for transport) simulations have been extracted on a hundred mesh slices perpendicular to the $x-$axis. Permeability, mean tortuosity, and mean shear rate have been calculated explicitly from the flow field results, while the dispersivity has been estimated with post-processing tools based on the method of moments and on the least square formulation of the inverse problem.

The results demonstrate the validity of the method, predicting the linear and non-linear regimes of Darcy's law with well-defined permeability and tortuosity constants in the first regime, and three different regimes for hydrodynamic dispersion [57]: the first one is dominated by the molecular dispersion (for low velocity and fine particles), then a region where

the mechanical and molecular dispersion are of the same order of magnitude, and finally a region where the dispersion depends linearly on the Peclét number, where the inertial effects dominate. This correlation for the hydrodynamic dispersion in terms of Peclét number is verified for the porous medium under study with the proposed simulation and upscaling tools.

The asymptotic dispersion regime is quickly reached and dispersion is well approximated by the Fickian hypothesis, even if the fluid velocity distributions are not Gaussian. Further studies will include a more careful characterization of the influence of the porous structures in terms of porosity and tortuosity and numerical upscaling of more complex macroscopic models will also be considered.

Acknowledgements

Funding for this work has been partially provided by the project PRIN 2008 "Produzione, stabilizzazione e trasporto di nano-particelle di ferro zero-valente per bonifica di acquiferi contaminati" of the Italian "Ministero dell'Istruzione, Università e Ricerca". Computational facilities have been partially offered by a European PRACE project, by Texas Supercomputing Center, by KAUST Visualization Lab and by KAUST HPC Lab. The authors acknowledge Dmitri Naumov for providing the code "SettleDyn", and Eleonora Crevacore for her work regarding the grid-independence analysis.

---

[1] J. Bear, *Dynamics of fluids in porous media* (Dover, 1988).

[2] A. M. Tartakovsky, Physical Review E **82**, 026302 (2010).

[3] S. Whitaker, *The method of volume averaging* (Springer, 1999).

[4] B. Berkowitz, J. Bear, and C. Braester, Water Resources Research **24**, 1225 (1995).

[5] J. Nordbotten, M. Celia, H. Dahle, and S. Hassanizadeh, Water Resources Research **43**, W08430 (2007).

[6] P. Forchheimer, Zeitschrift Verein Deutscher Ingenieure **45**, 1782 (1901).

[7] T. Tosco, D. L. Marchisio, F. Lince, and R. Sethi, Transport in Porous Media **96**, 1 (2013).

[8] R. Sethi, Journal of hydrology **400**, 187 (2011).

[9] A. D. Molfetta and R. Sethi, *Ingegneria degli acquiferi* (Springer, 2012).

[10] M. Rolle, G. Chiogna, D. L. Hochstetler, and P. K. Kitanidis, Journal of Contaminant Hydrology **153**, 51 (2013).

[11] R. D. Bauer, M. Rolle, S. Bauer, C. Eberhardt, P. Grathwohl, O. Kolditz, R. U. Meckenstock, and C. Griebler, Journal of Contaminant Hydrology **105**, 56 (2009).

[12] J. Hyman, P. Smolarkiewicz, and C. Winter, Physical Review E **86**, 056701 (2012).

[13] Y. Wang, Physical Review E **87**, 032144 (2013).

[14] B. Bijeljic, A. Raeini, P. Mostaghimi, and M. Blunt, Physical Review E **87**, 013011 (2013).

[15] P. Parthasarathy, P. Habisreuther, and N. Zarzalis, Chemical Engineering Science **90**, 242 (2013).

[16] B. Bijeljic, A. H. Muggeridge, and M. J. Blunt, Water Resources Research **40**, W1150101 (2004).

[17] G. Garmeh, R. Johns, and L. Lake, SPE Journal **14**, 559 (2009).

[18] S. Khirevich, A. Hltzel, and U. Tallarek, Communications in Computational Physics **13**, 801 (2013).

[19] R. S. Maier, D. M. Kroll, R. S. Bernard, S. E. Howington, J. F. Peters, and H. T. Davis, Physics of Fluids **12**, 2065 (2000).

[20] P. Mostaghimi, B. Bijeljic, and M. Blunt, SPE Journal **17**, 1131 (2012).

[21] S. Ovaysi and M. Piri, Journal of Contaminant Hydrology **124**, 68 (2011).

[22] Y. Zhu and P. J. Fox, Journal of Computational Physics **182**, 622 (2002).

[23] F. Augier, F. Idoux, and J. Delenne, Chemical Engineering Science **65**, 1055 (2010).

[24] M. J. Blunt, B. Bijeljic, H. Dong, O. Gharbi, S. Iglauer, P. Mostaghimi, A. Paluszny, and C. Pentland, Advances in Water Resources **51**, 197 (2013).

[25] G. Boccardo, D. Marchisio, and R. Sethi, Journal of Colloid and Interface Science **417**, 227 (2014).

[26] M. Balhoff, A. Mikelić, and M. F. Wheeler, Transport in Porous Media **81**, 35 (2010).

[27] K. Rajagopal, Mathematical Models and Methods in Applied Sciences **17**, 215 (2007).

[28] S. Whitaker, AIChE Journal **13**, 420 (1967).

[29] J. Bear and Y. Bachmat, Int. Union Geod. Geophys. Publ. **72** (1967).

[30] U. Hornung, *Homogenization and porous media* (Springer, 1997).

[31] M. Sahimi, *Flow and Transport in Porous Media and fractured rock* (Wiley, 2012).

[32] D. A. Benson, S. W. Wheatcraft, and M. M. Meerschaert, Water Resources Research **36**, 1403 (2000).

[33] J. H. Cushman and T. R. Ginn, Water Resources Research **36**, 3763 (2000).

[34] B. Berkowitz, A. Cortis, M. Dentz, and H. Scher, Reviews of Geophysics **44**, RG2003 (2006).

[35] A. M. Tartakovsky, D. M. Tartakovsky, and P. Meakin, Physical Review Letters **101**, 044502 (2008).

[36] R. Haggerty and S. M. Gorelick, Water Resources Research **31**, 2383 (1995).

[37] H. Gerke and M. v. Genuchten, Water Resources Research **29**, 305 (1993).

[38] A. Koponen, M. Kataja, and J. Timonen, Physical Review E **54**, 406 (1996).

[39] M. B. Clennell, Geological Society, London, Special Publications **122**, 299 (1997).

[40] A. Duda, Z. Koza, and M. Matyka, Physical Review E **84**, 036319 (2011).

[41] B. P. van Milligen and P. D. Bons, Physical Review E **85**, 011306 (2012).

[42] J. Feder, Journal of Theoretical Biology **87**, 237 (1980).

[43] M. Pilotti, Transport in Porous Media **33**, 257 (1998).

[44] C. Yeong and S. Torquato, Physical Review E **57**, 495 (1998).

[45] P.-E. Øren and S. Bakke, Transport in Porous Media **46**, 311 (2002).

[46] P.-S. Koutsourelakis and G. Deodatis, Journal of Engineering Mechanics **131**, 397 (2005).

[47] R. J. Adler and J. E. Taylor, *Random fields and geometry* (Springer, 2007).

[48] E. Coumans, Open source: bulletphysics.org (2006).

[49] G. Blöcher and G. Zimmermann, Computers & Geosciences **34**, 1827 (2008).

[50] J. Van Gumster, *Blender For Dummies* (Wiley, 2009).

[51] W. E. Lorensen and H. E. Cline, in *ACM Siggraph Computer Graphics* (ACM, 1987), vol. 21, pp. 163–169.

[52] P. Cignoni, M. Callieri, M. Corsini, M. Dellepiane, F. Ganovelli, and G. Ranzuglia, in *Eurographics Italian Chapter Conference* (The Eurographics Association, 2008), pp. 129–136.

[53] OpenCFD, *The Open Source CFD Toolbox, User Guide* (OpenCFD (ESI), 2013).

[54] J. H. Cushman, L. S. Bennethum, and B. X. Hu, Advances in Water Resources **25**, 1043 (2002).

[55] R. Aris, Proceedings of the Royal Society of London. Series A. Mathematical and Physical Sciences **235**, 67 (1956).

[56] J.-L. Auriault and P. Adler, Advances in Water Resources **18**, 217 (1995).

[57] M. Sahimi, AIChE Journal **41**, 229 (1995).